

# We are IntechOpen, the world's leading publisher of Open Access books Built by scientists, for scientists

6,500

Open access books available

176,000

International authors and editors

190M

Downloads

Our authors are among the

154

Countries delivered to

TOP 1%

most cited scientists

12.2%

Contributors from top 500 universities



WEB OF SCIENCE™

Selection of our books indexed in the Book Citation Index  
in Web of Science™ Core Collection (BKCI)

Interested in publishing with us?  
Contact [book.department@intechopen.com](mailto:book.department@intechopen.com)

Numbers displayed above are based on latest data collected.  
For more information visit [www.intechopen.com](http://www.intechopen.com)



Chapter

# Effects of Dimensionality Reduction for High-Efficiency Mg-Based Thermoelectrics

*Övgü Ceyda Yelgel*

## Abstract

Over the past decade, there has been significant interest in the field of thermoelectric materials (TEs) owing to their use in clean and sustainable energy sources for cooling and/or power generation applications. Especially,  $Mg_2XIV$  ( $XIV = Si, Ge, Sn$ ) based TEs are promising candidates for middle-temperature range energy conversion due to their high thermoelectric performance, environmentally harmless, abundant raw materials, non-toxicity, and relatively inexpensive cost of modules. In this book chapter, we present an overview of the theoretical background of the thermoelectric transport properties (Seebeck coefficient, electrical conductivity, thermal conductivity, and thermoelectric figure of merit  $ZT$ ) of magnesium-based bulk and low dimensional systems (i.e., quantum wells and quantum wires). A detailed description of the temperature-dependent Fermi level both in extrinsic and intrinsic regimes will be provided whereby it is the primary step in deriving the thermoelectric transport parameters of materials. Following the linearized Boltzmann transport equations temperature-dependent electronic transport properties (Seebeck coefficient, electrical conductivity, and electronic thermal conductivity) of materials under the energy-dependent relaxation time approximation will be defined. By employing Debye's isotropic continuum model within the single mode relaxation time approximation including various phonon relaxation rates contributed by different scattering mechanisms the lattice contribution to the thermal conductivity will be included.

**Keywords:** thermoelectric figure of merit, Mg-based thermoelectrics, thermoelectric transport properties, Boltzmann transport equation, thermal conductivity, phonon scattering mechanisms

## 1. Introduction

Due to the increasing world's demand for high-efficient clean energy researchers have been looking for environmentally friendly energy technologies. Non-renewable energy sources (nuclear power, coal, oil, and gas) have many disadvantages that can be listed as limited reserves, hazardous environmental risks, acid precipitation, and global climate change. Therefore, renewable energy sources determined as sourced either directly or indirectly from the Sun and solar energy have attracted much attention and scientific

studies have advanced rapidly in renewable energy technologies. As known heat and electricity are two different types of energy and thermoelectricity bridges between them. Thermoelectric materials can directly convert thermal energy (such as waste heat generated by automotive exhaust, domestic heating, and industrial processes) into electrical energy (and vice versa); this property makes them noteworthy for the development of sustainable energy-efficient technologies. Compared with other energy conversion technologies, thermoelectric devices have promising advantages such as having no moving parts, noiseless operation, long service life, stability, and less maintenance. Besides, it needs to be noted that the only major disadvantage of thermoelectric devices is their low efficiency for everyday common use compared to other energy conversion technologies. As summarized in **Figure 1**, thermoelectric devices can be extensively used in many fields such as power generators, cooling devices, sensors, space exploration, solar-based driven thermoelectric technologies, waste heat recovery from automobile engines, and energy harvesting and temperature control [1–6].

Different sectors contributing to huge amounts of waste heat energy (~66%), the biggest energy problem in the world right now, could be transformed to electrical energy via thermoelectric materials with the help of their ability to convert large amounts of wasted thermal energy into useful energy. **Figure 2a** shows the utilization of waste heat energy from different types of waste energy sources by thermoelectric generator.

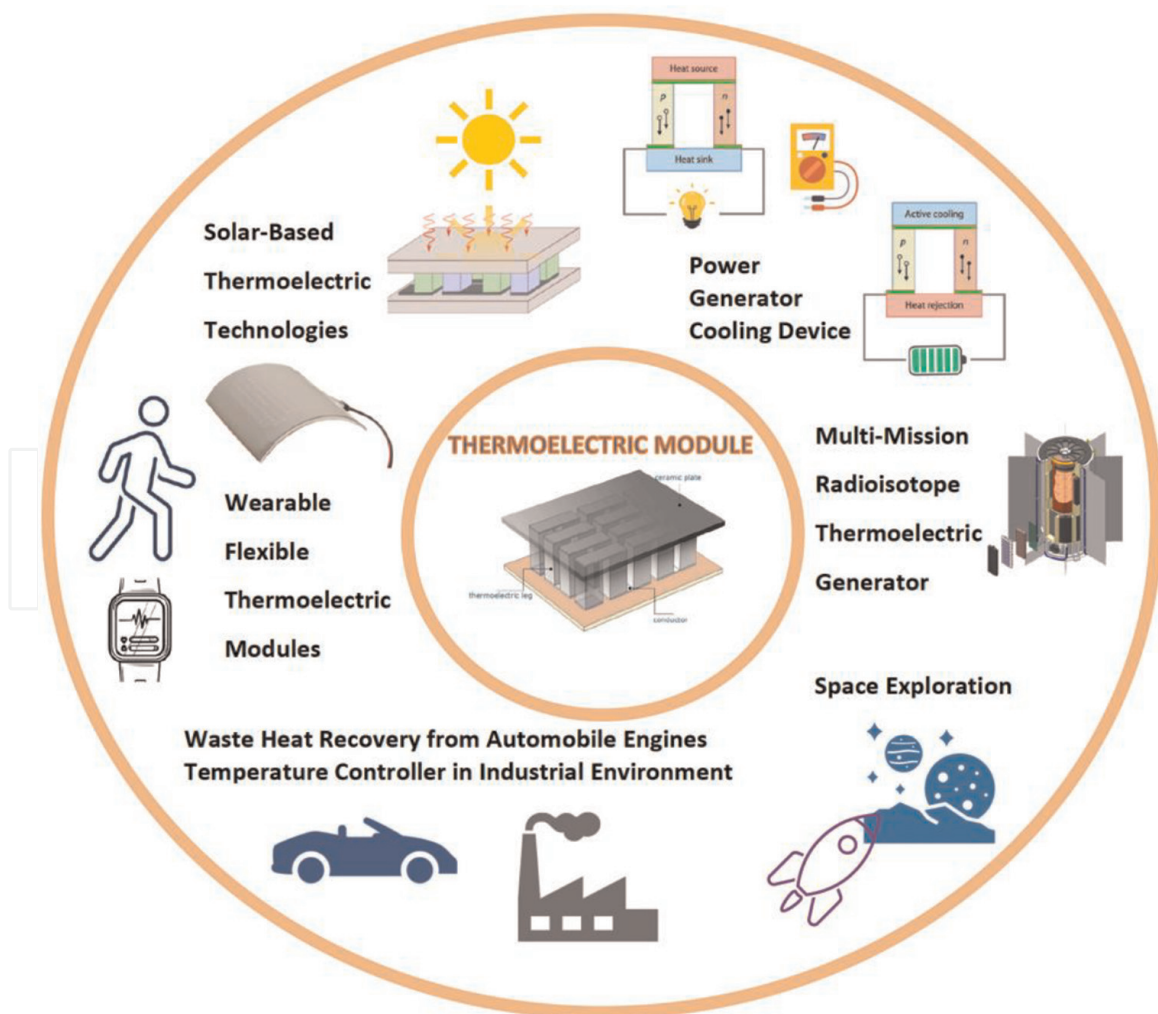


**Figure 1.** Overview of application fields of thermoelectric materials.

Thermoelectric generators are built of thermoelectric modules and a single module consists of a thermocouple. In **Figure 2b**, an operation of thermoelectric module working as a power generator mode is given. A single thermocouple generates a small thermoelectric force, and therefore to the formation of one module is used even so many thermocouples in this manner when the thermal energy is supplied the heat is directed to the thermoelectric modules in which a conversion of thermal energy into electricity. As shown in **Figure 3a**, a thermoelectric couple composed of an n-type (electrons are carriers) and a p-type (holes are carriers) semiconductor material connected through metallic electrical contact pads. Both power generation (Seebeck effect) and refrigeration (Peltier effect) can be accomplished using the same module.

The thermoelectric performance of the materials at a certain temperature is ranked by the dimensionless figure of merit  $ZT$ . Its definition is  $ZT = \frac{S^2 \sigma}{\kappa_{\text{total}}} T$  where  $T$  is the absolute temperature,  $S$  is the Seebeck coefficient,  $\sigma$  is the electrical conductivity, and  $\kappa_{\text{total}}$  is the total thermal conductivity ( $\kappa_{\text{total}} = \kappa_c + \kappa_{\text{bp}} + \kappa_{\text{ph}}$ ) which has contributions from carriers (i.e., from electrons for n-type materials or holes for p-type materials,  $\kappa_c$ ), electron-hole pairs (bipolar,  $\kappa_{\text{bp}}$ ), and phonons ( $\kappa_{\text{ph}}$ ), respectively. The material with a high  $ZT$  value has better thermoelectric energy conversion efficiency.

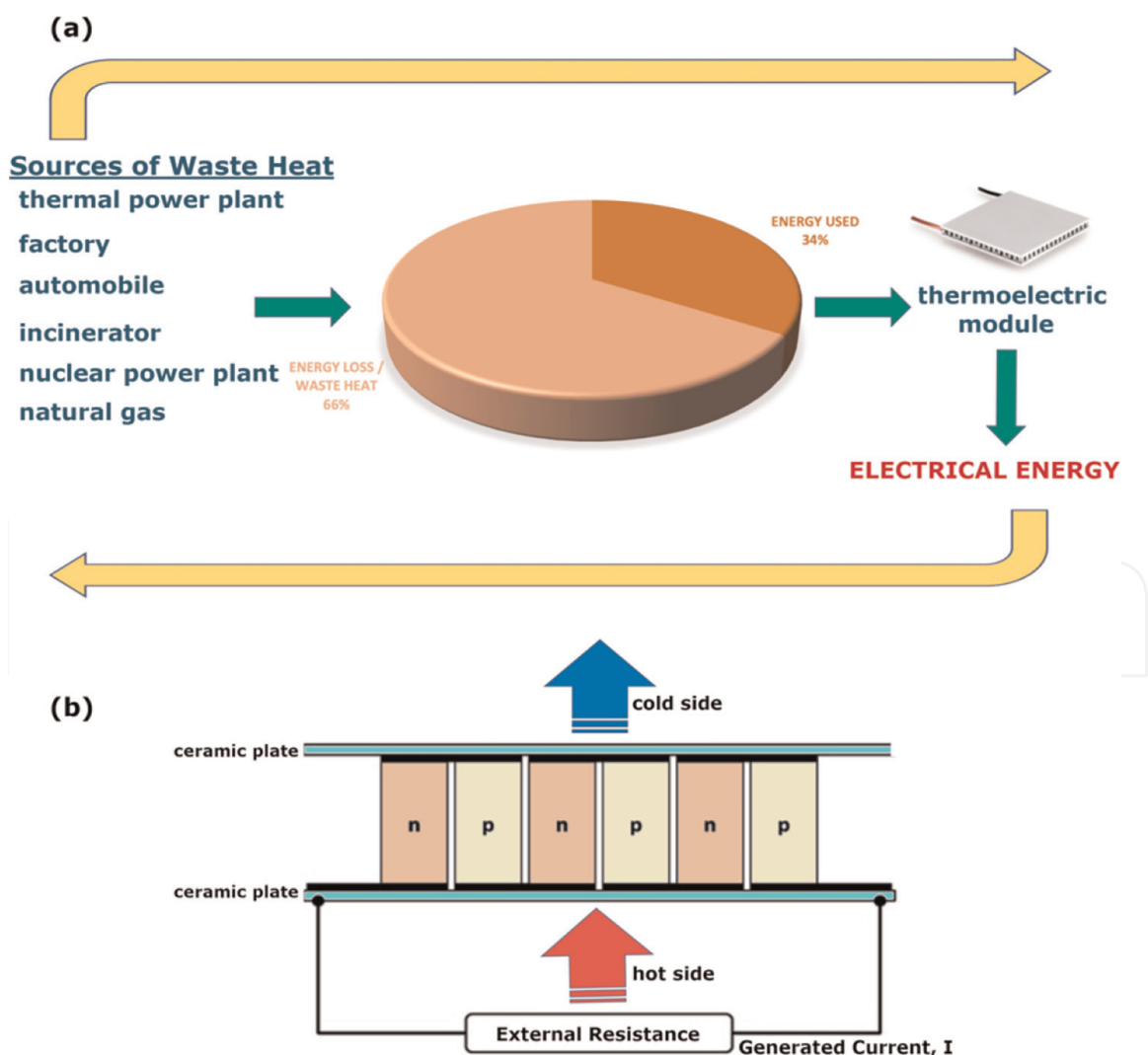


**Figure 2.**  
 (a) Utilization of waste heat energy from different types of waste energy sources by thermoelectric generator, and  
 (b) scheme and operation of thermoelectric module working as a power generator.

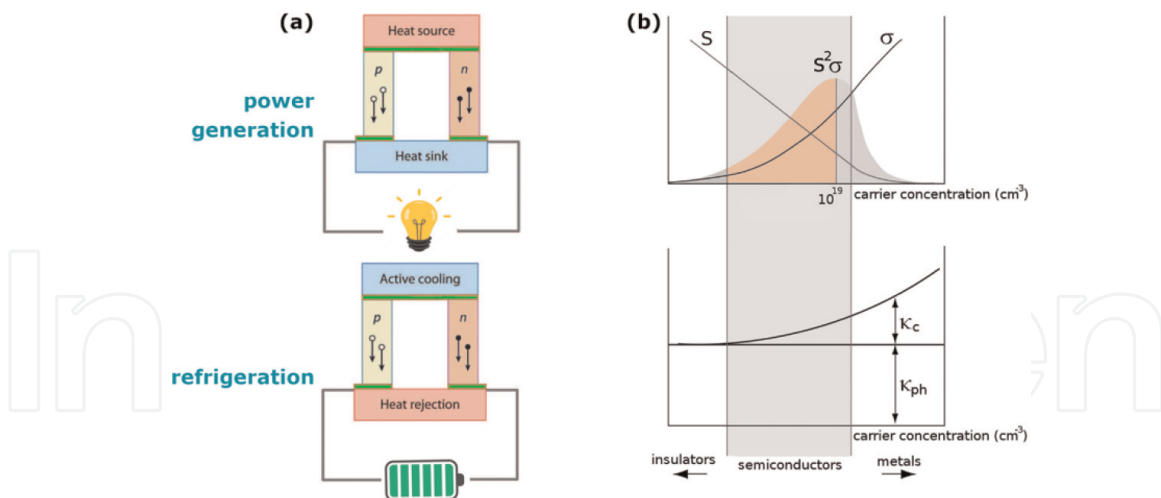


**Figure 3.**

(a) Operation principle of a power generator (Seebeck effect) and a refrigerator (Peltier effect), and (b) schematic presentation of carrier concentration dependence of electrical transport properties (Seebeck coefficient, electrical conductivity, carrier thermal conductivity) and thermal transport sourced from phonons.

Therefore, efficient thermoelectric materials need to have a large Seebeck coefficient to maximize the conversion of heat to electrical power; high electrical conductivity to minimize Joule heating; and low total thermal conductivity to retain heat at the junctions and maintain a large temperature gradient. However, as presented in **Figure 3b**, these thermoelectric transport properties are strongly coupled with each other and dependent on the material's band and crystal structure parameters. Owing to the complex interdependence among these properties, it is quite challenging to optimize  $ZT$  value and for this reason, the vast majority of research in this field has been focused on this issue. A desirable goal for everyday practical usage of the thermoelectric device is expected to have their efficiency in the range of  $ZT > 1.5$  and  $ZT > 2$  for power generation and thermoelectric cooling, respectively [7–9]. In the literature, until the 1990s, the highest value of  $ZT$  was found to be around 1 which means only 10% conversion efficiency [10–12]. In the last few years, on the other hand, the highest  $ZT$  values have been recorded with the help of using novel materials, following different processing techniques, and having new mechanisms [2, 13–16]. There are various strategies to improve thermoelectric efficiency; maximizing thermoelectric power factor ( $PF = S^2\sigma$ ) by following different methods such as convergence of electronic band valleys, carrier energy filtering, and generating resonant levels in electronic bands [13, 15, 17–22]; reducing total thermal conductivity with introducing new point defects by making alloys, embedding nano inclusion, anharmonicity, nano/mesoscale grain boundaries [2, 14, 23–28]. Among all these methods we must admit that in the thermoelectric literature Hicks and Dresselhaus made a revolutionary invention by proposing the use of low-dimensionalizing in thermoelectric devices and opened a new pathway in high-efficiency thermoelectric technologies in the early 1990s [29]. In the low dimensionalization method, reduced sizes of materials to the order of a nanometer in one or two directions are used (such as superlattices, nanowires, or quantum dots). Following this strategy allows enhancing  $ZT$  to a very large extent by optimizing electronic and thermal properties of materials in ways that are not possible in bulk materials. Also, the thermoelectric efficiency of traditional three-dimensional bulk materials can be improved with the help of the low-dimensionalization method. Low dimensional thermoelectric materials with unusual high  $ZT$  values (which can easily break the limits of unity) have

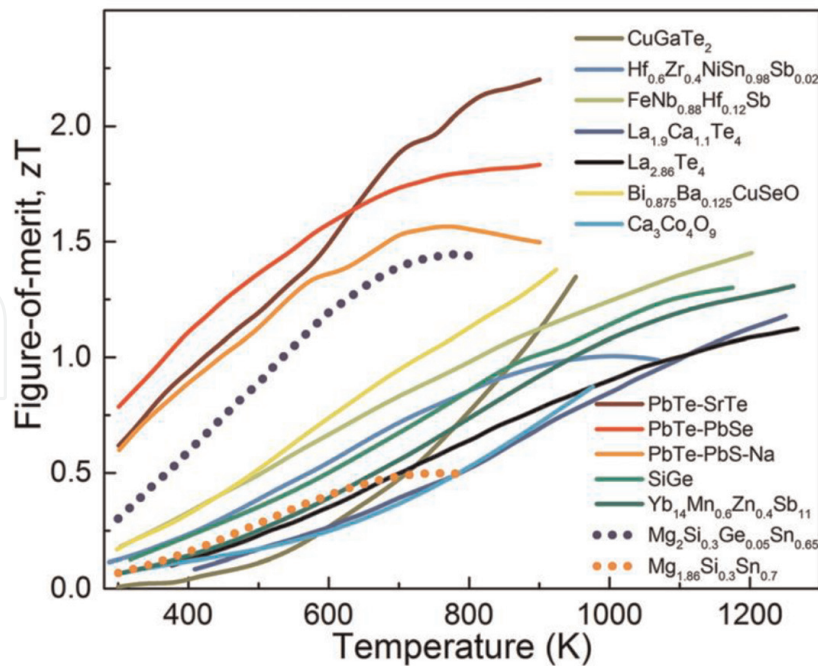


**Figure 4.** High-efficient thermoelectric materials working in the middle-to-high temperature range. Reproduced from Ref. [40] with permission from the Royal Society of Chemistry.

been reported by several groups [2, 13, 15, 17, 30–33]. Moreover, there have been significant improvements in portable electronics and intelligent society based on the internet of things (IoTs), and the internet of nano things (IoNTs) however rechargeable lithium-ion batteries are inconvenient for applications. At this point, by generating electricity from the temperature difference between the human body and the environment, high-efficiency nano-based thermoelectric materials can be an ideal solution to replace lithium-ion batteries in IoTs and IoNTs [34–39].

There are so many different thermoelectric materials however among all of them the materials working in the middle-temperature range (namely from 400 K to 800 K) are widely used for thermoelectric applications. Generally, in commercial practice  $\text{Bi}_2\text{Te}_3$ -,  $\text{PbTe}$ -,  $\text{CoSb}_3$ -, and  $\text{GeTe}$ -based thermoelectric compounds are mainly used whereas they have toxic constituent elements and are scarce [40–43]. The present market search for cheap, environmentally friendly, and non-toxic thermoelectric materials due to safety regulations. Compared to other middle-temperature thermoelectric materials Magnesium-based materials ( $\text{Mg}_2\text{X}$ ;  $\text{X} = \text{Si}, \text{Ge}, \text{Sn}$ ) have been regarded as promising candidates for high efficiency and large-scale application owing to their high availability, low-cost, reasonable high efficiency, non-toxicity, and low mass density. In **Figure 4**, the highest  $ZT$  values of the state-of-the-art medium-to-high temperature thermoelectric materials are given to compare with Mg-based thermoelectric materials.

$\text{Mg}_2\text{X}$  materials are intermetallic alloys that have been investigated for decades as high-efficiency thermoelectric candidates [44, 45].  $\text{Mg}_2\text{X}$  compounds crystallize in the cubic anti-fluorite structure (space group of  $Fm\bar{3}m$  #225) phase with X in face-centered cubic position and Mg in tetrahedral sites with three atoms per primitive unit cell in that one X atom is located at  $a(0\ 0\ 0)$  and 2 Mg atoms are located at  $a(0.25, 0.25, 0.25)$  and  $a(0.75, 0.75, 0.75)$ . The crystal structure model of  $\text{Mg}_2\text{X}$  and schematic illustration of the band structures of  $\text{Mg}_2\text{X}$  around  $\Gamma$  and X points are shown in **Figure 5a** and **b**, respectively.

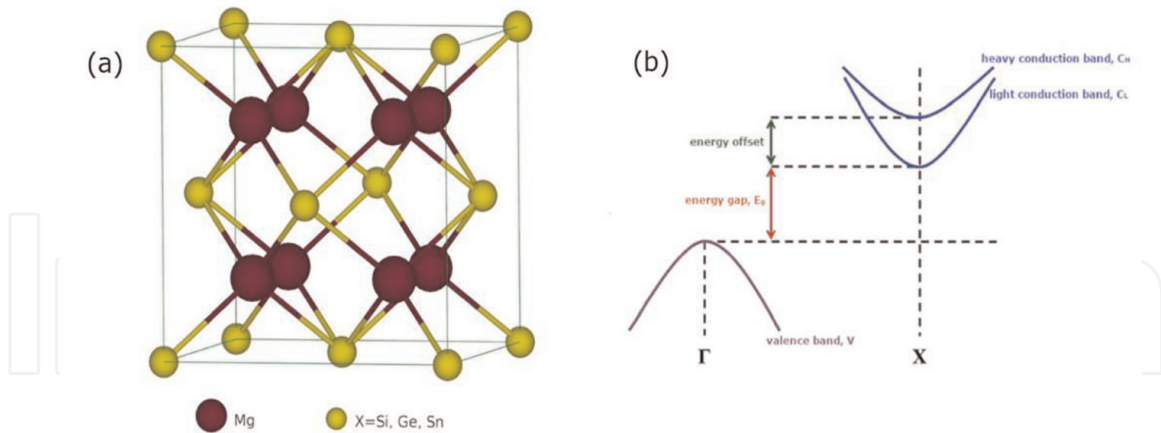


**Figure 5.** (a) Crystal structure model of  $Mg_2X$  ( $X = Si, Ge, Sn$ ), and (b) schematic illustration of  $Mg_2X$  around  $\Gamma$  and  $X$  points.

Properties/Parameters	$Mg_2Si$	$Mg_2Ge$	$Mg_2Sn$
$a$ ( $\text{\AA}$ )	6.338	6.385	6.765
$E_g$ (eV) at 0 K	0.77	0.74	0.35
$\Delta E$ (eV) at 0 K	0.4	0.58	0.16
Melting point (K)	1375	1388	1051
$\gamma$	1.32	1.38	1.27
$\kappa_{ph}$ ( $W\ m\ K^{-1}$ )	7.9	6.6	5.9

**Table 1.**

List of electronic (lattice parameters, band gaps, and energy offsets), physical (melting points), and phononic properties (Grüneisen parameter, and phonon thermal conductivity) of  $Mg_2X$  ( $X = Si, Ge, Sn$ ) binary alloys [46–48].

In addition to that, in **Table 1**, electronic and physical properties are listed for  $Mg_2X$ -based binary alloys.

The overview of the highest reported  $ZT$  values for Mg-based thermoelectric materials (in the form of binary, ternary, and quaternary n- and p-type doped) is illustrated in **Figure 6**.

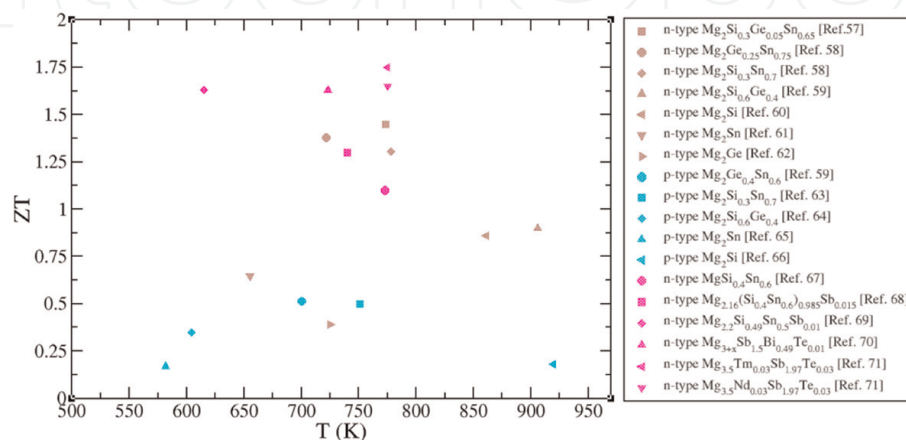


**Figure 6.** State-of-the-art  $ZT$  values for Mg-based thermoelectric materials from different works in the literature [49–63].

As stated above combining the advantages of using low-dimensionalization and Mg-based thermoelectric materials can lead to highly efficient thermoelectric applications. Despite this, in the literature, there have been very limited theoretical investigations of low-dimensional effects on thermoelectric transport properties of Mg-based materials in detail. Therefore, in this book chapter, unlike the related literature, a comprehensive explanation of the temperature-varied Fermi levels (both at extrinsic and intrinsic regimes) will first be presented for bulk and low-dimensional Mg-based materials. Then, by following the linearized Boltzmann transport equations temperature dependence of electronic transport properties (Seebeck coefficient, electrical conductivity, and carrier thermal conductivity) of bulk and low-dimensional Mg-based materials under the energy-dependent relaxation time approximation will be defined. Also, by employing Debye's isotropic continuum model within the single mode relaxation time approximation including various phonon relaxation rates contributed by different scattering mechanisms the lattice thermal contribution will be explained meticulously. By presenting a detailed theoretical background of the dimensionality effect on thermoelectric efficiency and highlighting the temperature dependencies of transport properties of low-dimensional systems we shed light on the challenges and perspectives for promoting the development of future Mg-based thermoelectric applications.

## 2. Thermoelectric transport properties of bulk and low-dimensional systems

The theory of transport properties in thermoelectric materials deals with the temperature dependence of electrical and thermal transport properties. Here, we introduce the theoretical background of thermoelectric transport properties in bulk and low-dimensional systems, respectively.

As stated in the above section, the dimensionless figure of merit includes three interdependent transport properties of  $S$ ,  $\sigma$ , and  $\kappa_{\text{total}}$  and which impedes the maximization of  $ZT$  in bulk systems. To avoid this problem, in 1993, Hicks and Dresselhaus examined the effects of using low-dimensional structures on the  $ZT$  with the assumption of parabolic bands and constant relaxation time in a one-band material [29]. To summarize Hicks and Dresselhaus' approach and describe the effects of dimensionalization as a bird's eye view, by defining a dimensional factor  $N$  ( $N = 1, 2$ , and  $3$  for 1 dimensional (1D), 2 dimensional (2D), and 3 dimensional (3D) systems, respectively) the dimensionality dependence of  $ZT$  can be written for the case of conduction along the  $x$  direction as [29, 64],

$$Z_N T = \frac{\frac{N}{2} \left( S_N \frac{F_{N/2}}{F_{N/2-1}} \zeta^* \right)^2 F_{N/2-1}}{\frac{1}{B_N} + \left( \frac{N+4}{2} \right) F_{N/2+1} - \beta_N \frac{F_{N/2}^2}{F_{N/2-1}}} \quad (1)$$

where  $\zeta^*$  is the reduced chemical potential,  $S_N = \frac{14-6N+N^2}{3}$ ,  $\beta_N = \frac{34-9N+2N^2}{6}$ , and the Fermi-Dirac function  $F_i$  is given by  $F_i(\zeta^*) = \int_0^\infty \frac{x^i dx}{\exp(x-\zeta^*)+1}$ . The material property dependent parameter  $B_N$  is expressed as,

$$B_N = \gamma_N \left( \frac{2k_B T}{\hbar^2} \right)^{N/2} \frac{k_B^2 T \mu_x}{e \kappa_{\text{ph}}} \quad (2)$$



where  $k_B$  is the Boltzmann constant and  $\hbar$  is the reduced Planck's constant,  $\gamma_1 = \frac{2}{\pi a^2} (m_x)^{1/2}$  for 1D systems,  $\gamma_2 = \frac{1}{2\pi a} (m_x m_y)^{1/2}$  for 2D systems, and  $\gamma_3 = \frac{1}{3\pi^2} (m_x m_y m_z)^{1/2}$  for 3D systems, respectively. Here  $m_x$ ,  $m_y$ , and  $m_z$  are the effective mass components for the x, y, and z directions,  $\mu_x$  is the mobility in the x direction, and  $a$  is the width of a 2D quantum well or 1D nanowire. From these equations, we can conclude that  $ZT$  depends on  $\zeta^*$  and  $B_N$  parameters. For bulk materials,  $ZT$  can be improved by optimizing  $\zeta^*$  with suitable doping and  $B_N$  with reducing  $\kappa_{ph}$  and/or increasing  $\mu_x$ . From the above equations, it is seen that in low-dimensional systems,  $ZT$  can be enhanced by adjusting the width/thickness of wells and wires, respectively. Decreasing the width/thickness of the quantum well or nanowire gives rise to boundary scattering mechanisms which lead to a dramatic reduction in phonon thermal conductivity. In **Figure 7**, the quantum well thickness and quantum wire diameter dependences of  $ZT$  are represented for quantum wells and wires of  $\text{Bi}_2\text{Te}_3$  fabricated along the x, y, and z directions [64].

After emphasizing the importance of using low-dimensional materials briefly, we can now move on to examine the detailed transport properties of thermoelectric materials both in bulk and low-dimensional structures to understand the detailed physical background behind these temperature-dependent transport properties and carrier scattering mechanisms. Based on the semiclassical model we follow the Boltzmann transport equation approach to investigate the thermoelectric transport phenomena quantitatively and explain how the temperature variations of carriers and phonons. All the electronic transport properties of thermoelectric materials are dependent on temperature-varied Fermi levels ( $E_F$ ) in extrinsic and intrinsic regimes. Therefore, simpler schemes leading to expressions for the Fermi level in bulk semiconductors have been given in the book by McKelvey [65],

$$E_F^{\text{ext}} (\text{n-type}) = \frac{1}{2}(E_c + E_d) + \frac{k_B T}{2} \ln \frac{N_d}{2U_c} - k_B T \sinh^{-1} \left[ \sqrt{\frac{U_c}{8N_d}} \exp\left(-\frac{\Delta E_i}{2k_B T}\right) \right] \quad (3)$$

$$E_F^{\text{ext}} (\text{p-type}) = \frac{1}{2}(E_a + E_v) + \frac{k_B T}{2} \ln \frac{N_a}{2U_v} - k_B T \sinh^{-1} \left[ \sqrt{\frac{U_v}{8N_d}} \exp\left(-\frac{\Delta E_i}{2k_B T}\right) \right] \quad (4)$$

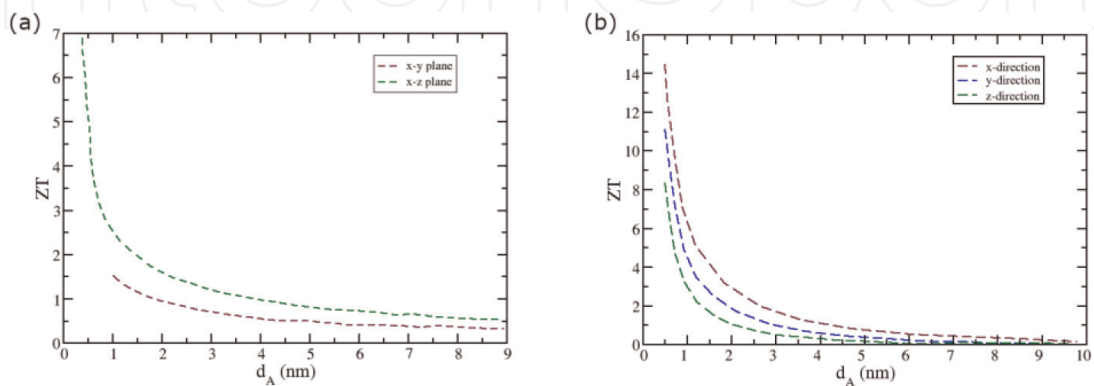


**Figure 7.** Enhanced  $ZT$  values as a function of (a) the quantum well thickness, and (b) the quantum wire diameter. Here quantum wells are fabricated in the x-y plane and the x-z plane while quantum wires are fabricated along the x, y, and z directions (data are read from Ref. [64]).

where  $E_c$  is the conduction band edge,  $E_v$  is the valence band edge,  $E_d$  is the donor energy level, and  $E_a$  is the acceptor energy level,  $\Delta E_i$  is given as  $(E_c - E_d)$  for the donor ionization and expressed as  $(E_a - E_v)$  for the acceptor ionization energies. Also,  $N_d$  and  $N_a$  are the concentrations of donor impurity and acceptor impurity atoms, respectively.  $U_c$  and  $U_v$  parameters are given as  $U_c = 2((m_n^* k_B T) / (2\pi\hbar^2))^{3/2}$  and  $U_v = 2((m_p^* k_B T) / (2\pi\hbar^2))^{3/2}$  where  $m_n^*$  is for the electron mass and  $m_p^*$  is for the hole mass. At high enough temperatures donors at the  $E_d$  or acceptors at the  $E_a$  levels become ionized and the material turns out to be an intrinsic semiconductor. The temperature dependence of EF for both types of doped semiconductors is expressed as [65],

$$E_F^{\text{int}}(\text{n - and p - types}) = \frac{1}{2}(E_v + E_c) + \frac{3}{4}k_B T \ln\left(\frac{m_p^*}{m_n^*}\right). \quad (5)$$

The temperature dependence of the Fermi level for semiconductors can be summarized as; in n-type doped semiconductors, the  $E_F$  is in the middle of the  $E_d$  and  $E_c$  at 0 K, and when the temperature rises the  $E_F$  first rises slowly and then decreases through the  $E_d$  and reaches the center of the gap; similarly, in p-type doped semiconductors the  $E_F$  is in the middle of the  $E_a$  and  $E_v$  at 0 K and when the temperature rises the  $E_F$  first goes down slightly and then increases through the  $E_a$ . For both types of doped semiconductors when the donor/acceptor levels are almost completely ionized the  $E_F$  approaches to  $E_F^{\text{int}}$ . Moreover, the energy dispersion function at the Brillouin zone center is determined as

$$E(k_x, k_y, k_z) = \frac{\hbar^2 k_x^2}{2m_x^*} + \frac{\hbar^2 k_y^2}{2m_y^*} + \frac{\hbar^2 k_z^2}{2m_z^*} \quad (6)$$

where  $k_x$ ,  $k_y$ , and  $k_z$  are the propagation vector component along the  $x$ ,  $y$ , and  $z$  axes, respectively. The effective mass tensor components of the constant energy surfaces are denoted as  $m_x^*$ ,  $m_y^*$ , and  $m_z^*$ .

In this book chapter, we consider low-dimensional systems as 2D quantum wells and 1D quantum wires and present the theoretical modeling of the temperature dependence of thermoelectric transport properties in these systems. First, in 2D quantum well systems, we assume that the system has B/A/B layers of material A (as a well material with  $n_A$  atomic layers of thickness  $a$  each and total thickness  $d_A$ ) and material B (as a barrier with  $n_B$  atomic layers of thickness  $b$  each and total thickness  $d_B$ ) also band gap differences materials A and B to confine the current carriers to the well material and system is grown in the  $z$ -direction. The electronic dispersion in the  $z$ -direction is given as,

$$E(k_x, k_y) = \frac{\hbar^2 k_x^2}{2m_x^*} + \frac{\hbar^2 k_y^2}{2m_y^*} + E_j, \quad (7)$$

where the quantum confinement term  $E_j$  in the  $j$ th quantum sublevel is expressed as

$$E_j = \frac{\hbar^2 \pi^2}{2m_z^* d_A^2} j. \quad (8)$$

Assuming the carrier concentration does not change whereas the well thickness varies and up to  $j$ th quantum sub-level is occupied by carriers the temperature variation of  $E_F$  for 2D quantum wells can be defined as

$$E_f^{\text{ext/int}}(2\text{D}_{\text{QWL}}) = E_f^{\text{ext/int}}(3\text{D}_{\text{BULK}}) - E_j. \quad (9)$$

in both extrinsic and intrinsic regimes [66]. Moreover, the energy band gap of this 2D system is given as

$$E_g(2\text{D}_{\text{QWL}}) = E_g(3\text{D}_{\text{BULK}}) + \frac{\hbar^2 \pi^2}{2d_A^2} \left( \frac{1}{m_{z,e}^*} + \frac{1}{m_{z,h}^*} \right) \quad (10)$$

where  $E_g(3\text{D}_{\text{BULK}}) = E_c - E_v$  and  $m_{z,e}^*$  and  $m_{z,h}^*$  are electrons and holes effective masses in the growth direction, respectively.

In 1D quantum wire systems, we assume that carrier confinement in the  $y$  and  $z$  directions and free-electron-like motion in the  $x$  direction also  $a$  is the width of the wire considered to have a square cross-section. The electronic dispersion relation for the 1D system is given as,

$$E(k_x) = \frac{\hbar^2 k_x^2}{2m_x^*} + E_{ij}, \quad (11)$$

where the quantum confinement terms  $E_{ij}$  in the  $i$ th and  $j$ th quantum sublevel are expressed as

$$E_{ij} = \frac{\hbar^2 \pi^2}{2m_y^* d_A^2} i + \frac{\hbar^2 \pi^2}{2m_z^* d_A^2} j, \quad (12)$$

with the width of the wire  $d_A$  assumed to have a square cross-section. Similar to 2D quantum wells, for 1D quantum wire systems the temperature dependence of  $E_F$  can be written as

$$E_f^{\text{ext/int}}(1\text{D}_{\text{QWR}}) = E_f^{\text{ext/int}}(3\text{D}_{\text{BULK}}) - E_{ij} \quad (13)$$

both in extrinsic and intrinsic regimes. Additionally, the band gap of 1D systems is given as

$$E_g(1\text{D}_{\text{QWR}}) = E_g(3\text{D}_{\text{BULK}}) + \frac{\hbar^2 \pi^2}{2d_A^2} \left( \frac{1}{m_{y,e}^*} + \frac{1}{m_{y,h}^*} \right) + \frac{\hbar^2 \pi^2}{2d_A^2} \left( \frac{1}{m_{z,e}^*} + \frac{1}{m_{z,h}^*} \right). \quad (14)$$

As shown in **Figure 8**, the carrier energy dependence of the density of states (DOS) per unit volume for a single band with the subband in bulk, quantum well, and quantum wire systems by assuming transport is along the direction of the  $x$ -axis. Compared to the 3D system  $g(E)$  enhances at  $E_0$  owing to the rise of carriers both with confinement effect in 2D and 1D systems.

The theoretical expressions of electronic transport properties for thermoelectric materials (namely the Seebeck coefficient, electrical conductivity, and electronic thermal conductivity) are explained by following the Boltzmann transport equation.

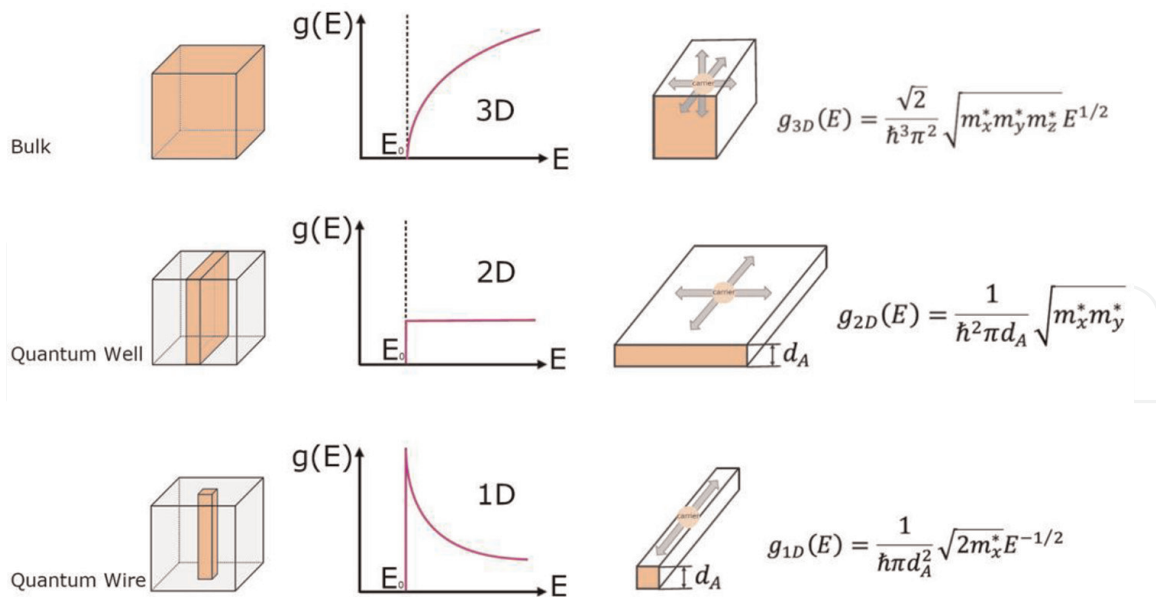


**Figure 8.** The electronic density of states for 3D, 2D, and 1D systems in relation to carrier energy ( $E_0$  corresponds to the energy at the bottom of the conduction band).

Presenting the theoretical background of each transport coefficient can help to understand the physical origin of these properties in relation to temperature and carrier concentration for bulk, quantum well, and quantum wire systems.

Assuming an isotropic solid within the nearly free electron/hole model under the consideration of an electric field and a temperature gradient is applied the thermoelectric transport properties can be determined by solving the linearized Boltzmann equation. Here, considering both heat and electricity currents flow in the  $x$ -direction, the electric current density  $i_x$  and the rate of flow of heat per unit cross-sectional area (carried by carriers)  $w_x$  are given [65–70].

$$i_x = \mp \int_0^\infty e v_x f(E) g(E) dE \quad (15)$$

$$w_x = \int_0^\infty v_x (E - E_f) f(E) g(E) dE \quad (16)$$

where  $-e$  is the electronic charge,  $v_x$  is the velocity of charge carriers in the  $x$ -direction for an isotropic conductor,  $f(E)$  is the Fermi distribution function,  $g(E)$  is the density of state function, and  $E - E_f$  represents the total energy transported by a carrier. At equilibrium, carrier distribution follows the Fermi Dirac statistics through  $f_0(E) = \left[ \exp\left(\frac{E - E_f}{k_B T}\right) + 1 \right]^{-1}$  where  $E_f$  is the Fermi energy. The above equations can be re-written by replacing  $f$  with  $f - f_0$  (since there is no transport  $i_x = w_x = 0$  when  $f = f_0$ ) as

$$i_x = \mp \int_0^\infty e v_x^2 \tau g(E) \frac{\partial f_0}{\partial E} \left( \frac{\partial E_f}{\partial x} + \frac{E - E_f}{T} \frac{\partial T}{\partial x} \right) dE \quad (17)$$

$$w_x = \pm \frac{E_f}{e} i_x + \int_0^\infty E v_x^2 g(E) \tau \frac{\partial f_0}{\partial E} \left[ \frac{\partial E_f}{\partial x} + \frac{E - E_f}{T} \frac{\partial T}{\partial x} \right] dE. \quad (18)$$

Here, the assumptions are  $\tau_x = \frac{\mu_x m_x^*}{e}$  with  $\mu_x$  is the carrier mobility in the  $x$ -direction and  $v_x^2 = \frac{2E}{3m_x^*}$ . By taking the condition  $i_x = 0$  as the Seebeck coefficient is written

$$S = -\frac{\Delta V}{\Delta T} = \frac{\varepsilon_x}{\nabla T} = \frac{1}{e} \frac{\partial E_f / \partial x}{\partial T / \partial x} \quad (19)$$

where the electric field  $\mathcal{E}_x$  is given as  $\varepsilon_x = \pm \frac{1}{e} \frac{\partial E_f}{\partial x}$  and  $S$  is expressed as

$$S = \pm \frac{1}{e} \left[ \int_0^\infty v_x^2 \tau_x g(E) \frac{\partial f_0}{\partial E} \frac{E - E_f}{T} dE / \int_0^\infty v_x^2 \tau_x g(E) \frac{\partial f_0}{\partial E} dE \right] \quad (20)$$

here + sign and – sign represent p- and n-type semiconductors, respectively. The electrical conductivity expression in the extrinsic regime can be defined by setting the temperature gradient as  $\partial T / \partial x = 0$  and expressed as

$$\sigma_{\text{ext}} = \frac{i_x}{\varepsilon_x} = - \int_0^\infty e^2 v_x^2 \tau_x g(E) \frac{\partial f_0}{\partial E} dE. \quad (21)$$

Additionally, in the intrinsic regime, the electrical conductivity of semiconductors is given by

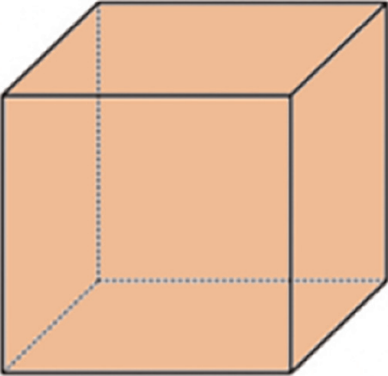
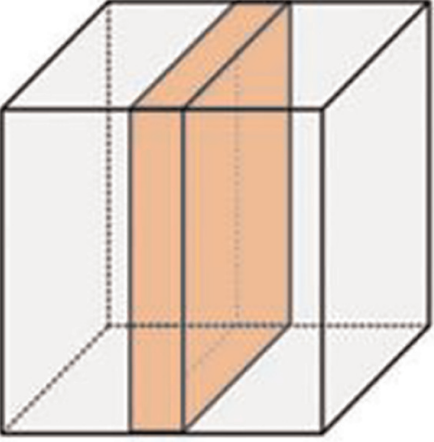
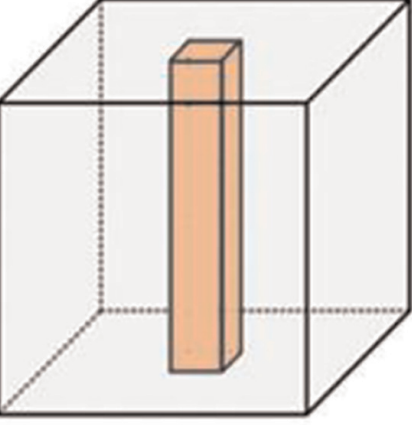
$$\sigma_{\text{int}} = e N_i (\mu_n + \mu_p) = A e^{-E_g / 2k_B T} \quad (22)$$

where  $N_i$  is the equilibrium carrier density,  $A$  is a temperature-independent adjustable parameter,  $\mu_n$  and  $\mu_p$  is the electron and hole mobility, respectively. Lastly, the total thermal conductivity is the sum of three contributions from carriers (electrons or holes), bipolar (electron-hole pairs), and phonons. The electronic thermal conductivity is related to the electrical conductivity by the Wiedemann-Franz law as  $\kappa_c = L\sigma T$  where  $L$  is the Lorenz number namely a relatively complex transport parameter. The carrier thermal conductivity comes from monopolar carriers (electrons or holes), is determined under the condition of  $i_x = 0$ , and is given as [71].

$$\kappa_c = -\frac{w_x}{\partial T / \partial x} = - \int_0^\infty v_x^2 E_g(E) \tau_x \frac{\partial f_0}{\partial E} \left( \frac{\partial E_f / \partial x}{\partial T / \partial x} + \frac{E - E_f}{T} \right) dE. \quad (23)$$

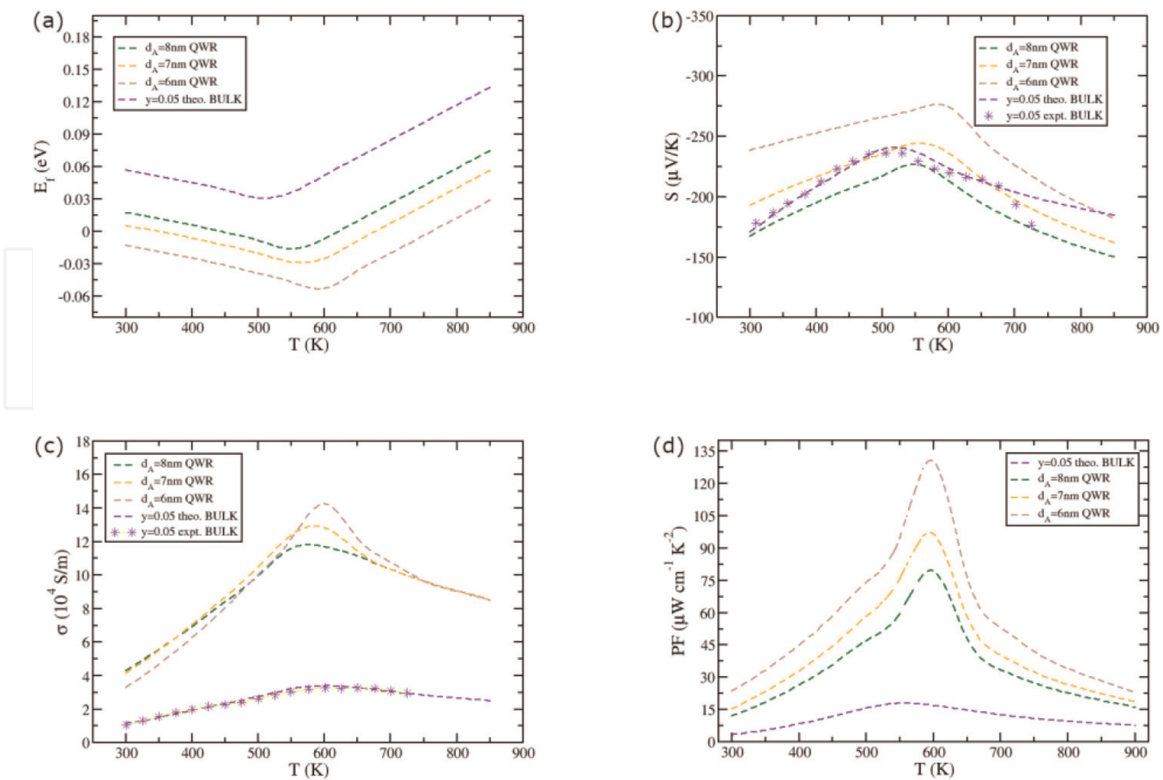
By determining these integrals we can now write expressions for the temperature dependence of electronic transport properties of 3D, 2D, and 1D systems. As the dimension of a system changes the above integrals need to be varied by the electronic density of states. In **Table 2**, the expressions for temperature-varied electronic transport properties are listed for bulk, quantum well, and wire systems.

In **Figure 9a–d**, the electronic transport properties of bulk and quantum wire structures (with wire widths taken as  $d_A = 6, 7,$  and  $8$  nm) of  $\text{Mg}_{3.2-y}\text{Co}_y(\text{Sb}_{0.3}\text{Bi}_{0.7})_{1.99}\text{Te}_{0.01}$  ( $y = 0.05$ ) are presented in the temperature ranges between 300 and 850 K. Additionally the experimental measurements of the temperature dependence of Seebeck coefficient and electrical conductivity results for bulk system reported by Ref. [72] are included to compare our theoretical results with experiments. As seen from the Fermi level results in **Figure 9a**, both bulk and quantum wire systems show extrinsic and intrinsic regimes in the whole temperature

Electronic transport property	3D bulk system	2D quantum well system	1D quantum wire system
			
$S$ (V/K)	$\pm \frac{k_B}{e} \left[ \frac{5F_{3/2}}{3F_{1/2}} - \frac{E_f}{k_B T} \right]$	$\pm \frac{k_B}{e} \left[ \frac{2F_1}{F_0} - \frac{E_f}{k_B T} \right]$	$\pm \frac{k_B}{e} \left[ \frac{3F_{1/2}}{F_{-1/2}} - \frac{E_f}{k_B T} \right]$
$\sigma_{\text{ext}}$ ( $\Omega \cdot \text{m}$ )	$\frac{1}{2\pi^2} \left( \frac{2k_B T}{\hbar^2} \right)^{3/2} (m_x^* m_y^* m_z^*)^{1/2} e\mu_x F_{1/2}$	$\frac{k_B T}{\hbar^2 \pi d_A} \sqrt{m_x^* m_y^*} e\mu_x F_0$	$\frac{\sqrt{2k_B T}}{\hbar^2 \pi d_A^2} \sqrt{m_x^*} e\mu_x F_{-1/2}$
$\sigma_{\text{int}}$ ( $\Omega \cdot \text{m}$ )	$A e^{-E_g^{3D}/2k_B T}$	$A e^{-E_g^{2D}/2k_B T}$	$A e^{-E_g^{1D}/2k_B T}$
$\kappa_c$ (W/K.m)	$\frac{\tau_x \hbar^2}{6\pi^2} \left( \frac{2k_B T}{\hbar^2} \right)^{5/2} \left( \frac{m_y^* m_z^*}{m_x^*} \right)^{1/2} k_B \left[ \frac{7}{2} F_{5/2} - \frac{25F_{3/2}^2}{6F_{1/2}} \right]$	$\frac{\tau_x k_B (2k_B T)^2 \sqrt{m_y^*}}{4\pi \hbar^2 d_A \sqrt{m_x^*}} \left[ 3F_2 - \frac{4F_1^2}{F_0} \right]$	$\frac{\tau_x k_B (2k_B T)^{3/2}}{\pi^2 \hbar d_A^2 \sqrt{m_x^*}} \left[ \frac{5F_{3/2}}{2} - \frac{9F_{1/2}^2}{2F_{-1/2}} \right]$

**Table 2.**

Temperature variation of electronic transport properties (Seebeck coefficient  $S$ , electrical conductivity in extrinsic  $\sigma_{\text{ext}}$  and intrinsic  $\sigma_{\text{int}}$  regimes, and carrier thermal conductivity  $\kappa_c$ ) of 3D, 2D, and 1D systems as a function of Fermi integrals described as  $F_i = \int_0^\infty x^i dx / (e^{x-\zeta^*} + 1)$  where energy ( $x$ ) and the reduced Fermi energy ( $\zeta^*$ ) of carriers normalized to the thermal energy are  $x = E/k_B T$  and  $\zeta^* = E_f/k_B T$ , respectively.


**Figure 9.**

The electronic transport properties of bulk  $\text{Mg}_{3.2-y}\text{Co}_y(\text{Sb}_{0.3}\text{Bi}_{0.7})_{1.99}\text{Te}_{0.01}$  ( $y = 0.05$ ) and its quantum wire structure with the wire widths of  $d_A = 6 \text{ nm}$ ,  $7 \text{ nm}$ , and  $8 \text{ nm}$ . The temperature variation of (a) Fermi level, (b) Seebeck coefficient, (c) electrical conductivity, and (d) power factor. Dashed lines are theoretical calculations and the star symbol is the experimental measurements read from ref. [72].

range. While the critical extrinsic-to-intrinsic turnover temperature is around 500 K for bulk sample, the temperature shifts to around 600 K for nanowire systems. In **Figure 9b**, the temperature variations of Seebeck coefficients are illustrated for both 3D and 1D systems. From these results, it is clearly seen that by decreasing the quantum wire width the maximum value of  $|S|$  can be improved from 241.1 ( $\mu\text{V/K}$ ) at 510 K upto 276.2 ( $\mu\text{V/K}$ ) at 593 K by using  $d_A = 6 \text{ nm}$  quantum wire instead of bulk structure. The temperature dependence of electrical conductivity for all systems is seen in **Figure 9c**. From theoretical calculations, it is seen that a dramatic enhancement can be gained in electrical conductivity by choosing low-dimensional systems. The maximum value of  $\sigma$  at 600 K is found to be  $3.4 \times 10^4 \text{ S/m}$  for bulk sample whereas it is found as  $14.2 \times 10^4 \text{ S/m}$  for  $d_A = 6 \text{ nm}$  quantum wire sample. Lastly, the temperature variation of the thermoelectric power factor for all samples is shown in **Figure 9d** and the highest PF values are  $18.5 \mu\text{W cm}^{-1} \text{ K}^{-2}$  at 550 K for the bulk sample and  $130.1 \mu\text{W cm}^{-1} \text{ K}^{-2}$  at 590 K for  $d_A = 6 \text{ nm}$  quantum wire sample.

In **Figure 10a** and **b**, the temperature dependence of electronic thermal conductivity of bulk and quantum wire structures (with different quantum wire widths taken as  $d_A = 6, 7,$  and  $8 \text{ nm}$ ) of  $\text{Mg}_{3.2-y}\text{Co}_y(\text{Sb}_{0.3}\text{Bi}_{0.7})_{1.99}\text{Te}_{0.01}$  ( $y = 0.05$ ) samples are represented in the temperature range of 300–850 K. From our theoretical calculations at room temperature it is found that while the minimum value of  $\kappa_c$  is  $0.051 \text{ W m}^{-1} \text{ K}^{-1}$  for bulk sample, a dramatic decrease is gained for quantum wire samples with the minimum value of  $\kappa_c$  is  $2.1 \times 10^{-5} \text{ W m}^{-1} \text{ K}^{-1}$  for  $d_A = 6 \text{ nm}$  sample. As seen from these temperature-varied electronic properties calculations, choosing low dimensional structured thermoelectric materials rather than bulk leads to enhanced

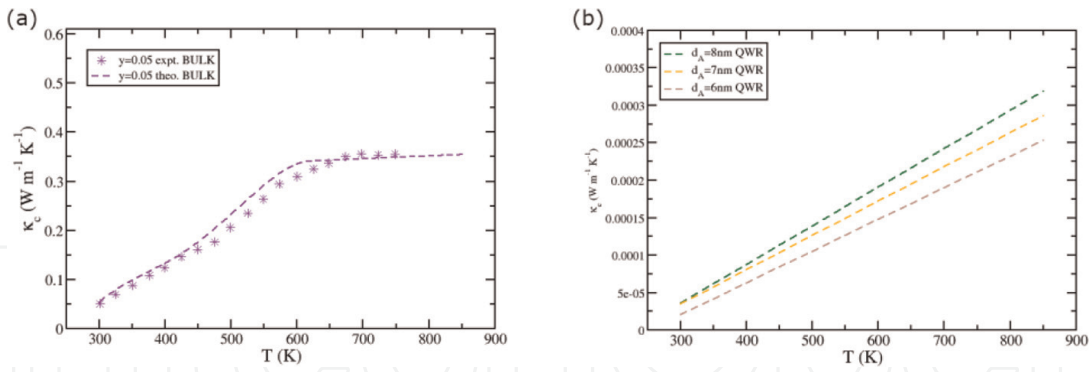


**Figure 10.** Temperature variation of the electronic thermal conductivity of (a) bulk Mg<sub>3.2-y</sub>Co<sub>y</sub>(Sb<sub>0.3</sub>Bi<sub>0.7</sub>)<sub>1.99</sub>Te<sub>0.01</sub> ( $y = 0.05$ ) and (b) its quantum wire structure with the wire widths of  $d_A = 6, 7, \text{ and } 8$  nm. Dashed lines are theoretical calculations and the star symbol is the experimental measurements done by Ref. [72].

thermoelectric power factor values which will help to get a more efficient thermoelectric material with a higher thermoelectric figure of merit.

The bipolar diffusion process is determined as at sufficiently high temperatures electron-hole pairs occur by excitation across the forbidden gap hence a continuous stream of charges flows in the direction of temperature gradient. High-efficiency thermoelectric materials are heavily doped narrow-band gap semiconductors and  $\kappa_{bp}$  plays a crucial role above room temperature in these small-band-gap thermoelectrics. In the assumption of an idealized semiconductor, has parabolic valence and conduction bands in that carriers only undergo acoustic mode lattice scattering, the  $\kappa_{bp}$  is defined by Glassbrenner and Slack

$$\kappa_{bp} = \frac{b}{(1+b)^2} \left[ \frac{E_g}{k_B T} + 4 \right]^2 \left[ \frac{k_B}{e} \right]^2 \sigma_{int} T \quad (24)$$

here the ratio of electron to hole mobility is determined with the parameter  $b$ . This expression is simplified by Yelgel and Srivastava [65].

$$\kappa_{bp} = F_{bp} T^p \exp(-E_g/2k_B T) \quad (25)$$

where  $F_{bp}$  and  $p$  are adjustable parameters vary with doping level and dopant type. When a material's dimension is changed to low dimensional structures in the expression of  $\kappa_{bp}$  the band gap property should be updated.

The most dominant contribution on the total thermal conductivity is sourced from lattice vibrations namely the phonon thermal conductivity  $\kappa_{ph}$  in degenerately doped and small-band-gap semiconductors. In thermal equilibrium condition, the average number of phonons in the  $q$ th mode and at temperature  $T$  is defined by the Bose-Einstein distribution function given as  $\bar{n}_q = \frac{1}{\exp(\hbar\omega(\mathbf{q})/k_B T) - 1}$  where  $\omega(\mathbf{q})$  is the angular frequency of phonons,  $\mathbf{q}$  is phonons wave vector, and  $\bar{n}_q$  is the average number of phonons in the  $q$ th mode. At low temperatures ( $\hbar\omega \gg k_B T$ ), there is an exponentially small probability for a phonon to be present with  $\bar{n} \simeq \exp(-\hbar\omega/k_B T)$ . Besides, as the temperature rises and reaches the high temperatures ( $k_B T \gg \hbar\omega$ ), the number of phonons increases linearly with temperature as  $\bar{n} \simeq k_B T/\hbar\omega$ . Following the linearized phonon Boltzmann equation, the phonon contribution can be expressed by employing Debye's isotropic continuum model within the single-mode relaxation time approximation as [73].



$$\kappa_{\text{ph}} = \frac{\hbar^2 q_D^5}{6\pi^2 k_B T^2} \sum_s c_s^4 \int_0^1 x^4 \tau_{qs} \bar{n}_{qs} (\bar{n}_{qs} + 1) dx \quad (26)$$

where  $\tau$  is the phonon relaxation time,  $c_s$  is the velocity of phonons for polarization branch  $s$ ,  $q_D$  is the Debye radius, and  $x = q/q_D$  is the reduced wave number. Within the Matthiessen's rule, the total contribution to the phonon lifetime is given by

$$\tau_{qs}^{-1} = \sum_i \tau_{qs,i}^{-1} \quad (27)$$

with  $\tau_{qs,i}^{-1}$  represents contributions from the  $i$ th scattering mechanism. Different scattering rates considered for Mg-based bulk and low-dimensional structured thermoelectric materials can be written as

$$\tau_{qs}^{-1}(\text{total}) = \tau_{qs}^{-1}(\text{bs}) + \tau_{qs}^{-1}(\text{md}) + \tau_{qs}^{-1}(\text{dp}) + \tau_{qs}^{-1}(\text{anh}) + \tau_{qs}^{-1}(\text{ims}) + \tau_{qs}^{-1}(\text{ids}) \quad (28)$$

where scattering mechanisms are sourced from boundary  $\tau_{qs}^{-1}(\text{bs})$ , mass-defect- $\tau_{qs}^{-1}(\text{md})$ , deformation potential  $\tau_{qs}^{-1}(\text{dp})$ , anharmonic  $\tau_{qs}^{-1}(\text{anh})$ , interface-mass-mixing  $\tau_{qs}^{-1}(\text{ims})$ , and interface-dislocation  $\tau_{qs}^{-1}(\text{ids})$ . Theoretical expressions for these phonon scattering mechanisms in bulk, quantum well, and quantum wire structured materials are listed in **Table 3**.

The temperature dependence of thermoelectric figure of merit for bulk  $\text{Mg}_{3.2-y}\text{Co}_y(\text{Sb}_{0.3}\text{Bi}_{0.7})_{1.99}\text{Te}_{0.01}$  ( $y = 0.05$ ) and its quantum wire structure with the wire widths of  $d_A = 6, 7, \text{ and } 8 \text{ nm}$  is represented in **Figure 11** with the experimental measurements reported by Ref. [72] for bulk  $\text{Mg}_{3.2-y}\text{Co}_y(\text{Sb}_{0.3}\text{Bi}_{0.7})_{1.99}\text{Te}_{0.01}$  ( $y = 0.05$ ) sample. As seen from our theoretical results, our thermoelectric transport modeling can successfully explain the experimental measurement of  $ZT$ ; while for the bulk sample the maximum value of  $ZT$  is theoretically found to be 1.07 at 550 K, its experimental measured value reported as 0.96 at 575 K by Ref. [72]. Additionally, using low dimensional quantum wires structure of  $\text{Mg}_{3.2-y}\text{Co}_y(\text{Sb}_{0.3}\text{Bi}_{0.7})_{1.99}\text{Te}_{0.01}$  ( $y = 0.05$ ) with different wire widths, the highest value of  $ZT$  at 600 K can be reached to 5.5, 3.7, and 2.7 for  $d_A = 6 \text{ nm}$ ,  $d_A = 7 \text{ nm}$ , and  $d_A = 8 \text{ nm}$ , respectively. Therefore low structured thermoelectric materials warrant dramatically enhanced thermoelectric efficiency compared to bulk materials.

In **Figure 12**, for the comparison the temperature-varied dimensionless figure of merits of n- and p-type  $\text{Zn}_4\text{Sb}_3$  and  $\text{Bi}_2\text{Te}_3$  nanowire-based thermoelectric materials, the state-of-the-art bulk and layered structured  $\text{Sn}(\text{Se},\text{S})$  and Mg-based thermoelectric materials and our theoretical Mg-based quantum wire systems are presented together.

## 2.1 Summary and future perspectives

Thermoelectric materials are very useful in various types of applications owing to their advantages as already discussed above. One of the current goals in thermoelectric research area is to find new and innovative thermoelectric material systems. During the last decades, a significant advancement in both theoretical and experimental studies has been achieved in the progress of high-efficient thermoelectric materials. Especially, recent advances in nanotechnology have brought with

Scattering mechanism	Expression
Boundary scattering	$\tau_{qs}^{-1}(\text{bs}) = c_s/L$ ; ( $L$ : phonon mean free path)
Mass defect scattering	$\tau_{qs}^{-1}(\text{md}) = \frac{\Gamma_{\text{md}}\Omega}{4\pi\bar{c}^3}\omega^4(qs)$ ; $\Gamma_{\text{md}} = \sum_i f_i \left(\frac{\Delta M_i}{\bar{M}}\right)^2$ ( $\bar{c}$ : average phonon speed; $f_i$ : the percentage of $i$ th isotope present in the crystal; $\Delta M_i = M_i - \bar{M}$ ; $\bar{M} = f_i M_i$ )
Deformation potential scattering	$\tau_{qs}^{-1}(\text{dp}) = \frac{3}{8\sqrt{\pi}} \frac{E_{\text{df}}^2}{\rho c_l^2 \hbar^4} (2m_c^* k_B T)^{3/2}$ ( $E_{\text{df}}$ : deformation potential; $\rho$ : mass density; $c_l$ : longitudinal acoustic phonon velocity; $m_c^*$ : effective mass of a charge carrier)
Anharmonic scattering	$\tau_{qs}^{-1}(\text{anh, BULK}) = \frac{\hbar q_D^5 \gamma^2}{4\pi\rho\bar{c}^2} \sum_{s's''e} c_s c_{s'}$ $\left[ \int dx' x'^2 x''_+ [1 - \epsilon + \epsilon(Cx + Dx')] \frac{\bar{n}_{q's'}(\bar{n}''_+ + 1)}{(\bar{n}_{qs} + 1)} + \frac{1}{2} \int dx' x'^2 x''_- [1 - \epsilon + \epsilon(Cx - Dx')] \frac{\bar{n}_{q's'}\bar{n}''_-}{\bar{n}_{qs}} \right]$ <p>(<math>\gamma</math>: Grüneisen constant; <math>x' = q'/q_D</math>; <math>x''_{\pm} = Cx \pm Dx'</math>; <math>\bar{n}_{\pm} = \bar{n}(x''_{\pm})</math>, <math>C = c_s/c_{s'}</math>; <math>D = c_{s'}/c_{s''}</math>)</p> $\tau_{qs}^{-1}(\text{anh, QWL}) = \tau_{qs}^{-1}(\text{anh, BULK})(n_A + n_B)^{2/3}$ <p>(<math>n_A</math>: number of well layers; <math>n_B</math>: number of barrier layers)</p> $\tau_{qs}^{-1}(\text{anh, QWR}) = 1/A(T)\omega^2$ $A(T) = \frac{k_B}{2\pi^2 c_{\text{ph}}^{\text{BULK}}} \int_0^{\omega_D} \frac{(\hbar\omega/k_B T)^2 e^{\hbar\omega/k_B T}}{(e^{\hbar\omega/k_B T} - 1)^2} d\omega$
Interface dislocation scattering	$\tau_{qs}^{-1}(\text{ids, QWL}) = \frac{\Gamma_{\text{ids}}\Omega}{8\pi\bar{c}^3}\omega^4$ $\Gamma_{\text{ids}} = \frac{2\beta'_0}{n_A + n_B} \sum_i \exp\left(-\left \frac{l_i - l_0}{d}\right \right) \left(\frac{\Delta M_i}{\bar{M}}\right)^2 \left[1 + \left(\frac{e_B^2}{e_A^2}\right)^2 + 1 + \left(\frac{e_B^2}{e_A^2}\right)^2\right]$ <p>(<math>\beta'_0</math>: the fraction of broken bonds in the interface region.)</p>
Interface mass-mixing scattering	$\tau_{qs}^{-1}(\text{ims, QWL}) = \frac{\Gamma_{\text{ims}}\Omega}{4\pi\bar{c}^3}\omega^4(qs)$ $\Gamma_{\text{ims}} = \frac{2\beta_0}{n_A + n_B} \sum_i \exp\left(-\left \frac{l_i - l_0}{d}\right \right) \left(\frac{\Delta M_i}{\bar{M}}\right)^2 \left[\left(1 - \frac{e_B^2}{e_A^2}\right)^2 + \left(1 - \frac{e_B^2}{e_A^2}\right)^2\right]$ <p>(<math>d</math>: interlayer distance; <math>l_i</math>: layer distance from interface; <math>l_0</math>: coordinate of the interface; <math>\beta_0</math>: mass-mixing fraction at the interface; <math>e_B/e_A</math> the ratio of the amplitudes of eigenvectors in materials B and A.)</p> $\frac{e_B}{e_A} = \frac{\left[\frac{1}{M_0} - \Delta\left(\frac{1}{M}\right)\right] \cos(l_z q_z)}{\left\{\left(\frac{1}{M_0}\right)^2 \cos^2(l_z q_z) + \left[\Delta\left(\frac{1}{M}\right)\right]^2 \sin^2(l_z q_z)\right\}^{1/2} - \Delta\left(\frac{1}{M}\right)}$ $\frac{1}{M_0} = \frac{1}{2} \left(\frac{1}{M_A} + \frac{1}{M_B}\right); \Delta\left(\frac{1}{M}\right) = \frac{1}{2} \left(\frac{1}{M_A} - \frac{1}{M_B}\right); l_z = d_A + d_B$

**Table 3.**  
 Expressions for different phonon scattering mechanisms [65, 73–76].

promising methods that cause fundamental mechanisms to get enhanced thermoelectric efficiencies. In particular, low dimensional quantum well and quantum wire systems are niche applications in electronics as micro- and nano-generators due to a lower energy requirements. Although a tremendous progress has been achieved in the past few years, a number of fundamental questions about theoretical background on thermoelectric transport properties in low-dimensional systems still need to be

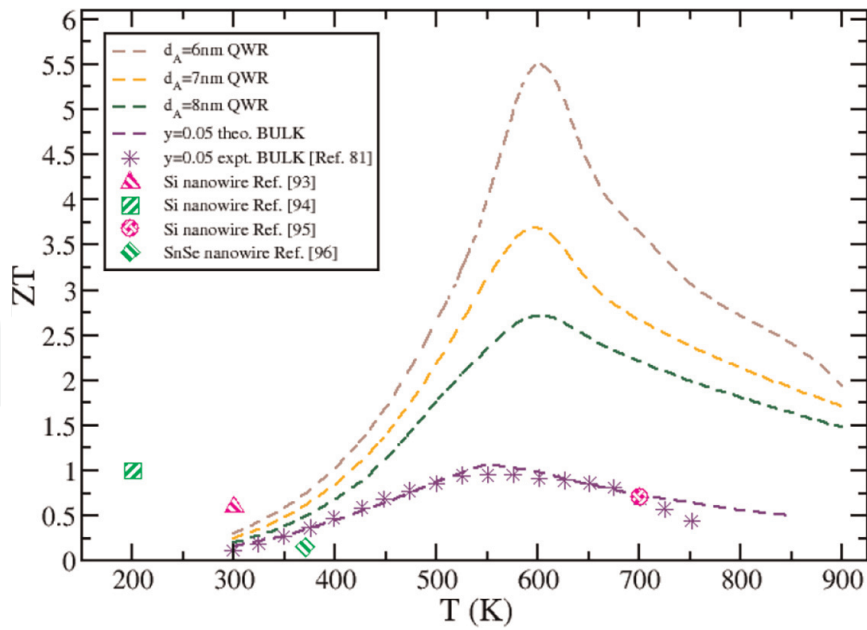


**Figure 11.** Temperature dependence of thermoelectric figure of merit  $ZT$  for bulk  $Mg_{3.2-y}Co_y(Sb_{0.3}Bi_{0.7})_{1.99}Te_{0.01}$  ( $y = 0.05$ ) and its quantum wire structure with the wire widths of  $d_A = 6, 7,$  and  $8$  nm. Dashed lines are our theoretical calculations and the symbols are the experimental measurements done by Refs. [72, 77–80].

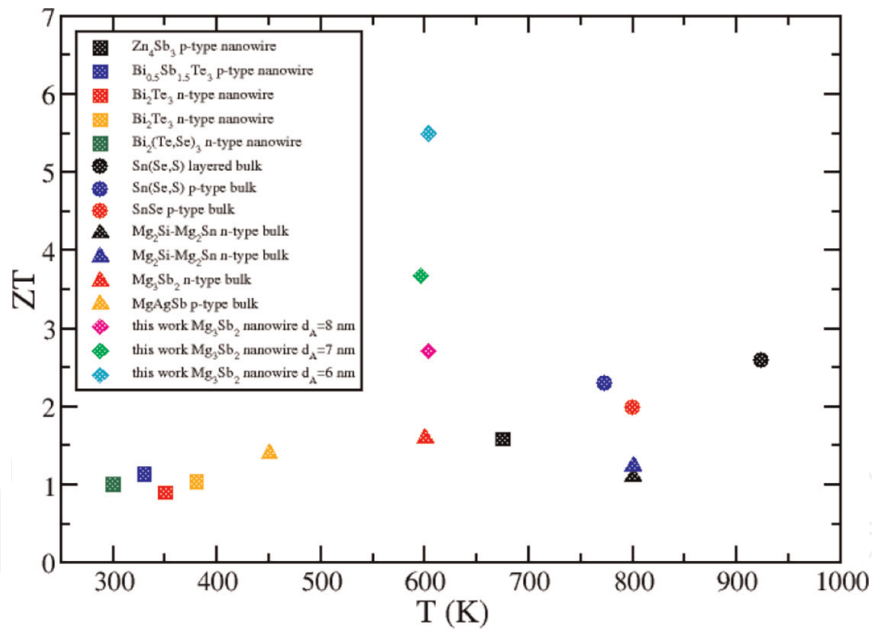


**Figure 12.** Comparison of the dimensionless figure of merit for Mg-based nanowire structured thermoelectric materials reported in this work with n- and p-type  $Zn_4Sb_3$  and  $Bi_2Te_3$  nanowire-based thermoelectric materials [81–85], and the state of the art bulk and layered structured  $Sn(Se,S)$  and Mg-based thermoelectric materials [25, 47, 86–90] in the literature.

investigated. Therefore, in this book chapter, we aim to explore the temperature variation of the thermoelectric transport properties of bulk and low dimensional materials systematically. We first start our theoretical investigation with the temperature-dependent Fermi level both in extrinsic and intrinsic regimes. Following the linearized Boltzmann transport equations the temperature variant electronic transport properties under the energy-dependent relaxation time approximation are

discussed for bulk and low dimensional systems. The thermal conductivity contributions from bipolar and phonon mechanisms are also discussed in detail. Phonon scattering rates sourced from boundaries, mass defects, anharmonicity, deformation potential, interface mass-mixing, and dislocation are given rigorously.

Among thermoelectric materials Mg-based thermoelectric materials have attracted intense interests owing to their enhanced  $ZT$  values at low-to-medium temperature range, together with the non-toxic, low-cost, earth abundant, low-density, and environmentally friendly. Here some major outlooks are listed:

- i. Mg-based compounds show highly degenerated conduction bands and can be alloyed and/or doped to form a wide range of compositions, providing enhanced  $ZT$  values.
- ii. Thermoelectric devices, applied for both power generation and refrigeration, have been successfully fabricated using Mg-based materials and can obtain high conversion efficiency.
- iii. Low-dimensional Mg-based systems (quantum wells and quantum wires) suggest even more enhanced  $ZT$  values than bulk systems with the help of quantum confinement effect.
- iv. As stated above, the main reason having higher  $ZT$  values in low-dimensional systems is having extremely low phonon thermal conductivity and high thermoelectric power factor at the same time.
- v. Since there are more intensely experimental studies in Mg-based thermoelectric materials in the literature it is essential to imply further theoretical investigations on Mg-based thermoelectric devices. Therefore, this chapter will be a possible guide to focus on thermoelectric transport properties of Mg-based bulk and low-dimensional systems.

Investigations on thermoelectric transport properties both in bulk and low-dimensional materials are becoming more prominent for solving today's energy challenges. Collaborations from scientists among different areas such as materials science, physics, and chemistry will have clear advantages in this global competition owing to interdisciplinary nature of thermoelectric research. In the light of these outlooks, developing Mg-based thermoelectric devices are well worthy of systematic study which should speed up their practical applications for energy harvesting. Hereby, the present book chapter comprises an overview of fundamental attainments and breakthroughs in experimental and theoretical thermoelectric research based on Mg-based materials. By presenting a detailed theoretical background on Mg-based 3D, 2D, and 1D systems it is clear that using low-dimensional systems certainly helps us to reach higher thermoelectric efficiencies. This also encourages experimentalists to use low dimensional structured Mg-based systems more often in new-generation thermoelectric devices.

## **Acknowledgements**

Ö. C. Y. acknowledges the support from the Scientific and Technical Research Council of Turkey (TÜBİTAK) (project code: 120F331).

## **Conflict of interest**

The authors declare no conflict of interest.

IntechOpen

## **Author details**


Övgü Ceyda Yelgel

Department of Electrical-Electronics Engineering, Recep Tayyip Erdoğan University,  
Rize, Turkey

\*Address all correspondence to: [oceyda.yelgel@erdogan.edu.tr](mailto:oceyda.yelgel@erdogan.edu.tr)

## **IntechOpen**

---

© 2023 The Author(s). Licensee IntechOpen. This chapter is distributed under the terms of the Creative Commons Attribution License (<http://creativecommons.org/licenses/by/3.0>), which permits unrestricted use, distribution, and reproduction in any medium, provided the original work is properly cited. 

## References

- [1] Rowe DM. Thermoelectrics Handbook. Boca Raton: CRC Press; 2005
- [2] Poudel B, Hao Q, Ma Y, Lan Y, Minnich A, Yu B, et al. High-thermoelectric performance of nanostructured bismuth antimony telluride bulk alloys. *Science*. 2008; **320**:634
- [3] Uher C. Materials Aspect of Thermoelectricity. USA Boca Raton: CRS Press Taylor & Francis Group; 2017
- [4] Kraemer D, Poudel B, Feng H-P, Caylor JC, Yu B, Yan X, et al. High performance flat-panel solar thermoelectric generators with high thermal concentration. *Nature Materials*. 2011; **10**:532
- [5] Mahan G, Sales B, Sharp J. Thermoelectric materials: New approaches to an old problem. *Physics Today*. 1997; **50**:42
- [6] Zhang Y, Chu Y, Xing W, Zheng L, Cao Y. Mechanical properties of thermoelectric Mg<sub>2</sub>Si using molecular dynamics simulations. *Mechanics of Advanced Materials and Structures*. 2017; **0**:1-6
- [7] DiSalvo FJ. Thermoelectric cooling and power generation. *Science*. 1999; **285**: 703
- [8] Bell LE. Cooling, heating, generating power, and recovering waste heat with thermoelectric systems. *Science*. 2008; **321**:1457
- [9] Szczech JR, Higgins JM, Jin S. Enhancement of the thermoelectric properties in nanoscale and nanostructured materials. *Journal of Materials Chemistry*. 2011; **21**:4037
- [10] Rowe DM. Applications of nuclear-powered thermoelectric generators in space. *Applied Energy*. 1991; **40**:241
- [11] Vandersande JW, Fleurial JP. Thermal management of power electronics using thermoelectric coolers. In: Fifteenth International Conference of Thermoelectrics Proceedings—ICT '96. Vol. **252**. Pasadena, CA. 1996. p. 255
- [12] Majumdar A. Materials science: Enhanced: Thermoelectricity in semiconductor nanostructures. *Science*. 2004; **303**:777
- [13] Heremans JP, Jovovic V, Toberer ES, Saramat A, Kurosaki K, Charoenphakdee A, et al. Enhancement of thermoelectric efficiency in PbTe by distortion of the electronic density of states. *Science*. 2008; **321**(5888):554
- [14] Biswas K, He J, Blum ID, Wu CI, Hogan TP, Seidman DN, et al. High-performance bulk thermoelectrics with all-scale hierarchical architectures. *Nature*. 2012; **489**(7416):414
- [15] Pei Y, Shi X, LaLonde A, Wang H, Chen L, Snyder GJ. Convergence of electronic bands for high performance bulk thermoelectrics. *Nature*. 2011; **473**(7345):66
- [16] Heremans JP, Thrusch CM, Morelli DT. Thermopower enhancement in lead telluride nanostructures. *Physical Review B*. 2004; **70**(11):115334
- [17] Liu W, Tan X, Yin K, Liu H, Tang X, Shi J, et al. Convergence of conduction bands as a means of enhancing thermoelectric performance of n-type Mg<sub>2</sub>Si<sub>1-x</sub>Sn<sub>x</sub> solid solutions. *Physical Review Letters*. 2012; **108**:166601

- [18] Zhao LD, Wu HJ, Hao SQ, Wu CI, Zhou XY, Biswas K, et al. All-scale hierarchical thermoelectrics: MgTe in PbTe facilitates valence band convergence and suppresses bipolar thermal transport for high performance. *Energy and Environmental Science*. 2013;**6**:3346
- [19] Banik A, Shenoy US, Anand S, Waghmare UV, Biswas K. Mg alloying in SnTe facilitates valence band convergence and optimizes thermoelectric properties. *Chemistry of Materials*. 2015;**27**:581
- [20] Bahk J-H, Bian Z, Shakouri A. Electron energy filtering by a nonplanar potential to enhance the thermoelectric power factor in bulk materials. *Physical Review B*. 2013;**87**:75204
- [21] Shakouri A, LaBounty C, Abraham P, Piprek J, Bowers JE. Enhanced thermionic emission cooling in high barrier superlattice heterostructures. *MRS Proceedings*. 1998;**545**:449
- [22] Zhang Q, Liao B, Lan Y, Lukas K, Liu W, Esfarjani K, et al. High thermoelectric performance by resonant dopant indium in nanostructured SnTe. *Proceedings of National Academy of Sciences*. 2013;**110**:13261
- [23] Biswas K, He J, Zhang Q, Wang G, Uher C, Dravid VP, et al. Strained endotaxial nanostructures with high thermoelectric figure of merit. *Nature Chemistry*. 2011;**3**:160
- [24] Zhao L-D, Hao S, Lo S-H, Wu C-I, Zhou X, Lee Y, et al. High thermoelectric performance via hierarchical compositionally alloyed nanostructures. *Journal of the American Chemical Society*. 2013;**135**:7364
- [25] Zhao L-D, Lo S-H, Zhang Y, Sun H, Tan G, Uher C, et al. Ultralow thermal conductivity and high thermoelectric figure of merit in SnSe crystals. *Nature*. 2014;**508**:373
- [26] Morelli DT, Jovovic V, Heremans JP. Intrinsically minimal thermal conductivity in cubic I–V–VI<sub>2</sub> semiconductors. *Physical Review Letters*. 2008;**101**:35901
- [27] Guin SN, Chatterjee A, Negi DS, Datta R, Biswas K. High thermoelectric performance in tellurium free p-type AgSbSe<sub>2</sub>. *Energy and Environmental Science*. 2013;**6**:2603
- [28] Guin SN, Pan J, Bhowmik A, Sanyal D, Waghmare UV, Biswas K. Temperature dependent reversible p–n–p type conduction switching with colossal change in thermopower of semiconducting AgCuS. *Journal of American Chemical Society*. 2014;**136**:12712
- [29] Hicks LD, Dresselhaus MS. Effect of quantum-well structures on the thermoelectric figure of merit. *Physical Review B*. 1993;**47**:12727
- [30] Venkatasubramanian R, Siivola E, Colpitts T, O’Quinn B. Thin-film thermoelectric devices with high room-temperature figures of merit. *Nature*. 2001;**413**:597
- [31] Harman TC, Taylor PJ, Walsh MP, LaForge BE. Quantum dot superlattice thermoelectric materials and devices. *Science*. 2002;**297**:2229
- [32] Harman T, Walsh M, Turner G. Nanostructured thermoelectric materials. *Journal of Electronic Materials*. 2005;**34**:L19
- [33] Heremans JP, Wiendlocha B, Chamoire AM. Resonant levels in bulk thermoelectric semiconductors. *Energy & Environmental Science*. 2012;**5**:5510

- [34] Miraz MH, Ali M, Excell PS, Picking RA. Review on internet of things (IoT). In: *Internet of Everything (IoE) and Internet of Nano Things (IoNT). Internet Technologies and Applications (ITA)*. New York, USA: IEEE; 2015. p. 219
- [35] Hiremath S, Yang G, Mankodiya K. Wearable internet of things: Concept, architectural components and promises for person-centered healthcare. In: *4th International Conference on Wireless Mobile Communication and Healthcare-Transforming Healthcare through Innovations in Mobile and Wireless Technologies (MOBIHEALTH)*. New York, USA: IEEE; 2014. p. 304
- [36] Hung NT, Nugraha AR, Yang T, Saito R. Confinement effect in thermoelectric properties of two-dimensional materials. *MRS Advances*. 2020;5(10):469
- [37] Haras M, Skotnicki T. Thermoelectricity for IoT—A review. *Nano Energy*. 2018;54:461
- [38] Suarez F, Nozariasbmarz A, Vashaee D, Öztürk MC. Designing thermoelectric generators for self-powered wearable electronics. *Energy & Environmental Science*. 2016;9(6):2099
- [39] Hyland M, Hunter H, Liu J, Veety E, Vashaee D. Wearable thermoelectric generators for human body heat harvesting. *Applied Energy*. 2016;182:518
- [40] Santos R, Yamini SA, Dou SX. Recent progress in magnesium-based thermoelectric materials. *Journal of Materials Chemistry A*. 2018;6:3328
- [41] Pei YZ, Wang H, Snyder GJ. Band engineering of thermoelectric materials. *Advanced Materials*. 2012;24:6125
- [42] Zhang Q, Li X, Kang Y, Zhang L, Yu D, He J, et al. High pressure synthesis of Te-doped  $\text{CoSb}_3$  with enhanced thermoelectric performance. *Journal of Materials Science: Materials in Electronics*. 2014;26:385
- [43] Gelbstein Y, Davidow J, Girard SN, Chung DY, Kanatzidis M. Controlling metallurgical phase separation reactions of the  $\text{Ge}_{0.87}\text{Pb}_{0.13}\text{Te}$  alloy for high thermoelectric performance. *Advanced Energy Materials*. 2013;3:815
- [44] Morris RG, Redin RD, Danielson GC. Semiconducting properties of  $\text{Mg}_2\text{Si}$  single crystals. *Physical Review*. 1958;109:1909
- [45] Heller MW, Danielson GC. Seebeck effect in  $\text{Mg}_2\text{Si}$  single crystals. *Journal of Physics and Chemistry of Solids*. 1962;23:601
- [46] Zaitsev VK, Fedorov MI, Gurieva EA, Eremin IS, Konstantinov PP, Samunin AY, et al. Thermoelectrics of n-type with  $ZT > 1$  based on  $\text{Mg}_2\text{Si}$ - $\text{Mg}_2\text{Sn}$  solid solutions. In: *ICT 2005 24<sup>th</sup> International Conference on Thermoelectrics*. 2005. p. 204
- [47] Zaitsev VK, Fedorov MI, Gurieva EA, Eremin IS, Konstantinov PP, Samunin AY, et al. Highly effective  $\text{Mg}_2\text{Si}_{1-x}\text{Sn}_x$  thermoelectrics. *Physical Review B*. 2006;74:045207
- [48] Zhou Z, Han G, Lu X, Wang G, Zhou X. High-performance magnesium-based thermoelectric materials: Progress and challenges. *Journal of Magnesium and Alloys*. 2022;10:1719
- [49] Tani J, Kido H. Thermoelectric properties of Bi-doped  $\text{Mg}_2\text{Si}$  semiconductors. *Physica B: Condensed Matter*. 2005;364:218



- [50] Gao HL, Zhu TJ, Zhao XB, Deng Y. Influence of Sb doping on thermoelectric properties of  $Mg_2Ge$  materials. *Intermetallics*. 2015;**56**:33
- [51] Mars K, Ihou-Mouko H, Pont G, Tobola J, Scherrer H. Thermoelectric properties and electronic structure of Bi- and Ag-doped  $Mg_2Si_{1-x}Ge_x$  compounds. *Journal of Electronic Materials*. 2009;**38**:1360
- [52] Zhang Q, Yin H, Zhao XB, He J, Ji XH, Zhu TJ, et al. Thermoelectric properties of n-type  $Mg_2Si_{0.6-y}Sb_ySn_{0.4}$  compounds. *Physica Status Solidi A*. 2008;**205**:1657
- [53] Liu W, Kim HS, Chen S, Jie Q, Lv B, Yao M, et al. N-type thermoelectric material  $Mg_2Sn_{0.75}Ge_{0.25}$  for high power generation. In: *Proceedings of the National Academy of Sciences of U.S.A.* 2015;**112**:3269
- [54] Yin K, Su X, Yan Y, You Y, Zhang Q, Uher C, et al. Optimization of the electronic band structure and the lattice thermal conductivity of solid solutions according to simple calculations: A canonical example of the  $Mg_2Si_{1-x-y}Ge_xSn_y$  ternary solid solution. *Chemistry of Materials*. 2016;**28**:5538
- [55] An T-H, Park C, Seo W-S, Choi S-M, Kim I-H, Kim S-U. Enhancement of p-type thermoelectric properties in an  $Mg_2Sn$  system. *Journal of Korean Physical Society*. 2012;**60**:1717
- [56] Ihou-Mouko H, Mercier C, Tobola J, Pont G, Scherrer H. Thermoelectric properties and electronic structure of p-type  $Mg_2Si$  and  $Mg_2Si_{0.6}Ge_{0.4}$  compounds doped with Ga. *Journal of Alloys and Compounds*. 2011;**509**:6503
- [57] Zhang Q, Cheng L, Liu W, Zheng Y, Su X, Chi H, et al. Low effective mass and carrier concentration optimization for high performance p-type  $Mg_{2(1-x)}Li_{2x}Si_{0.3}Sn_{0.7}$  solid solutions. *Physical Chemistry Chemical Physics*. 2014;**16**:23576
- [58] De Boor J, Saparamadu U, Mao J, Dahal K, Müller E, Ren Z. Thermoelectric performance of Li doped, p-type  $Mg_2(Ge,Sn)$  and comparison with  $Mg_2(Si,Sn)$ . *Acta Materialia*. 2016;**120**:273
- [59] Zhang Q, He J, Zhu TJ, Zhang SN, Zhao XB, Tritt TM. High figures of merit and natural nanostructures in  $Mg_2Si_{0.4}Sn_{0.6}$  based thermoelectric materials. *Applied Physics Letters*. 2008;**93**:102109
- [60] Liu W, Tang XF, Li H, Yin K, Sharp J, Zhou XY, et al. Enhanced thermoelectric properties of n-type  $Mg_{2.16}(Si_{0.4}Sn_{0.6})_{1-y}Sb_y$  due to nano-sized Sn-rich precipitates and an optimized electron concentration. *Journal of Materials Chemistry*. 2012;**22**:13653
- [61] Ning H, Mastrorillo GD, Grasso S, Du B, Mori T, Hu C, et al. Enhanced thermoelectric performance of porous magnesium tin silicide prepared using pressure-less spark plasma sintering. *Journal of Materials Chemistry A*. 2015;**3**:17426
- [62] Ozen M, Yahyaoglu M, Candolfi C, Veremchuk I, Kaiser F, Burkhardt U, et al. Enhanced thermoelectric performance in  $Mg_{3+x}Sb_{1.5}Bi_{0.49}Te_{0.01}$  via engineering microstructure through melt-centrifugation. *Journal of Materials Chemistry A*. 2021;**9**:1733
- [63] Zhang JW, Song LR, Iversen BB. Probing efficient n-type lanthanide dopants for  $Mg_3Sb_2$  thermoelectrics. *Advanced Science*. 2020;**7**:2002867
- [64] Mao J, Liu Z, Ren Z. Size effect in thermoelectric materials. *NPJ Quantum Materials*. 2016;**1**:16028

- [65] Yelgel ÖC, Srivastava GP. Thermoelectric properties of n-type  $\text{Bi}_2(\text{Te}_{0.85}\text{Se}_{0.15})_3$  single crystals doped with CuBr and  $\text{SbI}_3$ . *Physical Review B*. 2012;**85**:125207
- [66] Yelgel ÖC, Srivastava GP. Thermoelectric properties of  $\text{Bi}_2\text{Se}_3/\text{Bi}_2\text{Te}_3/\text{Bi}_2\text{Se}_3$  and  $\text{Sb}_2\text{Te}_3/\text{Bi}_2\text{Te}_3/\text{Sb}_2\text{Te}_3$  quantum well systems. *Philosophical Magazine*. 2014;**94**:2072
- [67] Ziman JM. *Electrons and Phonons: The Theory of Transport Phenomena in Solids*. Great Britain: Oxford University Press; 2001
- [68] Richard F. *Semiconductor Physics and Applications*. Great Britain: Oxford University Press; 2000
- [69] Tritt TM. *Thermal Conductivity: Theory, Properties, and Applications*. New York: Kluwer Academic/Plenum Publishers; 2004
- [70] Yu PY, Cardona M. *Fundamentals of Semiconductors : Physics and Materials Properties*. London: Springer; 2010
- [71] Wilson AH. *The Theory of Metals*. Great Britain: Cambridge University Press; 2011
- [72] Chen Y, Wang C, Ma Z, Li L, Li S, Wang J. Improved thermoelectric performance of n-type  $\text{Mg}_3\text{Sb}_2\text{-Mg}_3\text{Bi}_2$  alloy with Co element doping. *Current Applied Physics*. 2021;**21**:25
- [73] Srivastava GP. *The Physics of Phonons*. Bristol: Adam Hilger; 1990
- [74] Yelgel ÖC. Chapter6: Recent Advances on  $\text{Mg}_2\text{X}^{\text{IV}}$  based Thermoelectric Materials: A Theoretical Approach. U.S.A: John Wiley & Sons, Inc; 2019
- [75] Landry ES, McGaughey AJH. Effect of interfacial species mixing on phonon transport in semiconductor superlattices. *Physical Review B*. 2009;**79**:75316
- [76] Hepplestone SP, Srivastava GP. Theory of interface scattering of phonons in superlattices. *Physical Review B*. 2010;**82**:144303
- [77] Al H, Chen R, Delgado RD, Liang W, Garnett EC, Najarian M, et al. Enhanced thermoelectric performance of rough silicon nanowires. *Nature*. 2008;**451**(7175):163
- [78] Al B, Bunimovich Y, Tahir-Kheli J, Yu JK, Goddard WA III, Heath JR. Silicon nanowires as efficient thermoelectric materials. *Nature*. 2008;**451**(7175):168
- [79] Yang L, Huh D, Ning R, Rapp V, Zeng Y, Liu Y, et al. High thermoelectric figure of merit of porous Si nanowires from 300 to 700 K. *Nature Communications*. 2021;**12**:3926
- [80] Hernandez JA, Ruiz A, Fonseca LF, Pettes MT, Yacaman MJ, Benitez A. Thermoelectric properties of SnSe nanowires with different diameters. *Scientific Reports*. 2018;**8**:11966
- [81] Liu Y-B, Zhou S-M, Yuan X-Y, Lou S-Y, Gao T, Shi X-J, et al. Synthesis and high-performance thermoelectric properties of beta- $\text{Zn}_4\text{Sb}_3$  nanowires. *Materials Letters*. 2012;**84**:116
- [82] Li L, Xu S, Li G. Enhancement of thermoelectric properties in Bi–Sb–Te alloy nanowires by pulsed electrodeposition. *Energy Technology*. 2015;**3**:825
- [83] Chen C-L, Chen Y-Y, Lin S-J, Ho JC, Lee P-C, Chen C-D, et al. Fabrication and characterization of electrodeposited bismuth telluride films and nanowires.

Journal of Physical Chemistry C. 2010;  
**114**:3385

[84] Zhang G, Kirk B, Jauregui LA, Yang H, Xu X, Chen YP, et al. Rational synthesis of ultrathin n-type Bi<sub>2</sub>Te<sub>3</sub> nanowires with enhanced thermoelectric properties. *Nano Letters*. 2011;**12**:56

[85] Tan M, Deng Y, Wang Y. Ordered structure and high thermoelectric properties of Bi<sub>2</sub>(Te, Se)<sub>3</sub> nanowire array. *Nano Energy*. 2014;**3**:144

[86] Peng KL, Zhang B, Wu H, Cao XL, Li A, Yang DF, et al. Ultra-high average figure of merit in synergistic band engineered Sn<sub>x</sub>Na<sub>1-x</sub>Se<sub>0.9</sub>S<sub>0.1</sub> single crystals. *Materials Today*. 2018;**21**:501

[87] Peng KL, Lu X, Zhan H, Hui S, Tang XD, Wang GW, et al. Broad temperature plateau for high ZTs in heavily doped p-type SnSe single crystals. *Energy & Environmental Science*. 2016;**9**:450

[88] Tan XJ, Liu W, Liu HJ, Shi J, Tang XF, Uher C. Multiscale calculations of thermoelectric properties of n-type Mg<sub>2</sub>Si<sub>1-x</sub>Sn<sub>x</sub> solid solutions. *Physical Review B*. 2012;**85**:205212

[89] Zhang JW, Song LR, Sisti M, Tolborg K, Iversen BB. Chemical bonding origin of the unexpected isotropic physical properties in thermoelectric Mg<sub>3</sub>Sb<sub>2</sub> and related materials. *Nature Communications*. 2018;**9**:4716

[90] Zhao HZ, Sui JH, Tang ZJ, Lan YC, Jie Q, Kraemer D, et al. High thermoelectric performance of MgAgSb based materials. *Nano Energy*. 2014;**7**:97